Compact localized currents in flat bands with broken time-reversal symmetry

Rohit Kishan Ray [1, 2, *] Carlo Danieli [3, †] Alexei Andreanov [1, 4, ‡] and Sergej Flach [1, 4, 5, §]

[1] *Center for Theoretical Physics of Complex Systems, Institute for Basic Science, Daejeon 34126, Republic of Korea*
[2] *Department of Material Science and Engineering, Virginia Tech, Blacksburg, VA 24061, USA*
[3] *Istituto dei Sistemi Complessi, Consiglio Nazionale delle Ricerche, Via dei Taurini 19, 00185 Rome, Italy*
[4] *Basic Science Program, Korea University of Science and Technology, Daejeon 34113, Republic of Korea*
[5] *Centre for Theoretical Chemistry and Physics, The New Zealand Institute for Advanced Study (NZIAS), Massey University Albany, Auckland 0745, New Zealand*

(Dated: December 1, 2025)

We develop a systematic framework for constructing all-bands-flat (ABF) lattice Hamiltonians that explicitly break time-reversal symmetry (TRS). By threading magnetic flux through disconnected polygonal plaquettes and applying local entangling unitary transformations, we map plaquettes onto families of ABF models in one, two, and three dimensions. This procedure preserves the flux configuration while converting semi-detangled geometries into ABF lattices with nontrivial hopping structure. The resulting flat bands admit compact localized states (CLSs) whose support includes both the flux-threaded plaquettes and auxiliary sites introduced by the unitary transformations. In these TRS-broken constructions, the CLSs host localized circulatory currents whose magnitude depends on the applied flux. We further extend the framework to lattices with coexisting flat and dispersive bands, illustrating cases with both orthogonal and non-orthogonal CLSs. Our results provide a controlled route for generating dispersionless lattices supporting flux-induced local currents.

I. INTRODUCTION

Flat bands (FBs), *i.e.*, completely dispersionless energy spectra across the entire Brillouin zone, represent a remarkable class of electronic and photonic structures in condensed-matter physics and optics [1–7]. This absence of dispersion in lattice systems with short-range hopping causes the FB eigenstates to be non-zero only within a finite region due to destructive wave interference [8]. Hence, these states are referred to as compact localized states (CLSs). Interest in flat-band networks stems from their extreme sensitivity to perturbations, which gives rise to unconventional phenomena and a variety of nontrivial phases. Furthermore, FBs have been experimentally realized in a number of setups, from photonic waveguides [9–11] to ultra-cold atoms [12, 13], electrical circuits [14, 15] and acoustic [16, 17] meta-materials.

Since the inception of flat-bands [18–20], one of the most active areas of research has been the generation and the classification of FB lattices. Generating protocols developed over the years include methods based on chiral symmetry [19], origami schemes [21], repetition of mini-arrays [22], local symmetries [23], among many others [24–26]. A more systematic approach emerged from realizing that FBs can be generated by assuming a specific CLS profile and and fine-tuning the Hamiltonian networks that support them. This CLS-based approach not only yielded systematic flat-band generators in various dimensions [27–29], but also provided a pathway for an exhaustive classification of FBs. FBs indeed can be classified according to the orthogonality and completeness of the CLS set [30]. In general, CLSs form a linearly independent set of non-orthogonal states. In certain cases however the CLS set (i) turns into an orthonormal set [31]; or (ii) becomes a linearly dependent set. The latter class, which exists only for $D \geq 2$ spatial dimensions is also known as a singular flat band [5, 32–34]. In this case, the linear dependence of the CLS enforces that at least one the remaining dispersive bands touches the flat band.

A notable case of orthonormal FBs is when a lattice completely lacks dispersion — *i.e.*, all spectral Bloch bands are flat. Such systems are known as all-bands-flat (ABF) lattices. This scenario was introduced by Vidal *et.al.*, demonstrating that certain lattices threaded with fine-tuned magnetic flux feature exclusively flat bands [35, 36]. In this case, since all eigenstates are compact, any initially localized state will remain confined within a finite region— a phenomenon known as caging, which leads to a complete suppression of transport. The elimination of the single-particle transport mechanisms offers a fertile platform for investigating strongly correlated phases in the interacting case, from nonlinear caging [37–39] to many-body CLSs [40–42], quantum scars [43–46], and exact many-body flat band localization [47–49]. ABFs have also been experimentally realized with photonic waveguides [50–55], photonics [56], Fock space [57], cold atoms [58, 59], acoustic metamaterials [60], electric [15, 61] and superconducting [62] circuits.

We focus our attention on ABF lattices where time-reversal symmetry (TRS) is explicitly broken by magnetic flux. This focus is motivated by experiments where intrinsic magnetic fields were used to break the TRS in systems featuring nearly flat bands, leading to anomalous

* rkray@vt.edu
† carlo.danieli@cnr.it
‡ alexei.pcs@fastmail.org
§ sflach@ibs.re.kr

quantum hall effect [63, 64]. Furthermore, it has been demonstrated that introducing multiple fluxes can fine-tune photonic lattices into ABF regime while breaking TRS [65]. These developments raise several fundamental questions that motivate the present work: (i) can ABF lattices with broken TRS be systematically constructed, (ii) can this construction be extended to lattices supporting both flat and dispersive bands; and (iii) do the broken TRS induce localized currents in the CLS. In this work, we address these questions by developing a systematic scheme for constructing ABF models with broken TRS. The scheme builds on the local detangling properties characteristic of ABF lattices [39]. We construct explicit parametric families of such lattices in one, two, and three dimensions, and show that their CLSs support localized circulating currents whose magnitude depends on the applied magnetic flux. We further extend the framework to generate systems featuring coexisting flat and dispersive bands, illustrating examples with both orthogonal and non-orthogonal CLSs.

This paper is organized as follows. In Section II, we present the theoretical background. Section III details our construction method for engineering TRS-broken ABF models in 1D, 2D, and 3D, and demonstrates the resulting localized currents. In Section IV, we extend this discussion to lattices with coexisting flat and dispersive bands. Finally, Section V summarizes our findings and presents the conclusions.

II. TIME REVERSAL SYMMETRY IN HAMILTONIAN LATTICES

Let us consider a D dimensional lattice with ν bands (*i.e.* ν sites per unit-cell) described by an Hermitian Hamiltonian

$$\begin{aligned} H = &\sum_{\mathbf{m}} \sum_{\mu,\eta} [H_0]_{\mu,\eta} \, |\mathbf{m},\mu\rangle\langle\mathbf{m},\eta| \\ &+ \sum_{j} \sum_{\langle\mathbf{m},\mathbf{m}'\rangle_{s,j}} \sum_{\mu,\eta} [H_j^s]_{\mu,\eta} \, |\mathbf{m},\mu\rangle\langle\mathbf{m}',\eta| + \text{h.c.} \end{aligned} \tag{1}$$

The basis states $|\mathbf{m},\mu\rangle = a^\dagger_{\mathbf{m},\mu}|\varnothing\rangle$ are defined through the creation and annihilation operators $a^\dagger_{\mathbf{m},\mu}$ and $a_{\mathbf{m},\mu}$. The multi-index $\mathbf{m} \in \mathbb{Z}^D$ locates a unit cell within the lattice and the index $1 \leq \mu \leq \nu$ labels sites within each cell. The wave function is then expressed as $|\Psi\rangle = \sum_{\mathbf{m},\mu} \psi_{\mathbf{m},\mu} |\mathbf{m},\mu\rangle$. The Bravais lattice is defined by the primitive lattice translation vectors $\vec{a}_j$ for $1 \leq j \leq D$. The square matrix H_0 of size ν defines the unit cell profile, while the square matrices H_j^s define the hopping between s^{th} order-neighboring unit cells $\langle\mathbf{m},\mathbf{m}'\rangle_{s,j}$ at distance $|\mathbf{m}-\mathbf{m}'| = s$ along the vectors $\vec{a}_j$. Here we consider only finite range hopping between unit cells, $s < +\infty$, and finite number of Bloch bands, $\nu < +\infty$. The eigenvalue problem of the Hamiltonian H in Eq. (1) is $E|\Phi\rangle = H|\Phi\rangle$. Using the Bloch space representation $|\Psi\rangle = e^{\mathrm{i}\mathbf{k}\cdot\boldsymbol{m}}|\Phi\rangle$ for the wave vector $\mathbf{k}$ yields ν Bloch bands given by $\{E_\mu(\mathbf{k})\}_{\mu=1}^{\nu}$.

Let us now introduce the concept of time-reversal symmetry for Hamiltonian lattices. An Hamiltonian H acting on a Hilbert space $\mathcal{H}$ is time-reversal symmetric (TRS) if there exist an anti-unitary time-reversal operator $\mathcal{T}$ such that [66, 67]

$$\mathcal{T} H \mathcal{T}^{-1} = H. \tag{2}$$

The anti-unitary time-reversal operator $\mathcal{T}$ can be written as a composition of two operators as — $\mathcal{T} = \mathcal{U}\mathcal{K}$ where $\mathcal{U}$ is a unitary rotation and $\mathcal{K}$ is the standard complex conjugation. In case of spinless Hamiltonians (the focus of our work) we have $\mathcal{U} = \mathbb{I}$ and the time-reversal operator reduces to $\mathcal{T} = \mathcal{K}$. In our context, TRS yields a $\mathbf{k} \to -\mathbf{k}$ symmetry in the Bloch energy bands, which is typically broken in the absence of TRS. Importantly, time-reversal symmetry is not generically preserved under arbitrary unitary transformations. When a Hamiltonian is transformed as $H' = \boldsymbol{U} H \boldsymbol{U}^\dagger$, a necessary and sufficient condition for TRS preservation is that the operator $\mathcal{W} := \boldsymbol{U}^\dagger \mathcal{T} \boldsymbol{U} \mathcal{T}^{-1}$ commutes with H(see Appendix A). In the case of spinless Hamiltonians, it can be shown that the above condition reduces to $\boldsymbol{U} = \boldsymbol{U}^*$. Therefore, for a unitary drawn at random from the full unitary group $\mathrm{U}(n)$, TRS is almost surely broken unless: (i) we specifically restrict $\boldsymbol{U}$ to be a real (orthogonal) matrix, or (ii) $\boldsymbol{U}$ is such that the transformed Hamiltonian $H' \neq H'^*$ [68] and $\boldsymbol{U}^\dagger \mathcal{T} \boldsymbol{U} \mathcal{T}^{-1}$ commutes with H [69] (see Appendix A).

III. ALL-BANDS-FLAT LATTICES WITH BROKEN TIME REVERSAL SYMMETRY

In this section, we focus on constructing Hamiltonian lattices H in Eq. (1) where each of the ν Bloch bands is independent of momentum $\mathbf{k}$ over the entire Brillouin zone, $E_\mu(\mathbf{k}) = \text{const}$ for $1 \leq \mu \leq \nu$. This class of lattice networks lacking any band dispersion is called all-band-flat (ABF). This complete flattening of the spectral bands is highly nontrivial, as all eigenstates are macroscopically degenerate and are spatially compact, hence preventing any single particle transport along the lattice — a phenomenon that is also known as caging. The flat band eigenstates are called compact localized states (CLSs).

Following Ref. 39, a representation of an ABF lattice with Hamiltonian H in Eq. (1) featuring both non-zero intra-cell matrix H_0 and inter-cell hopping matrices H_j^s is called *Non-Detangled* (ND) [47]. In this case the values of the hopping profile encoded in the matrices H_0 and H_j^s are fine-tuned to impose destructive interference — hence, resulting in the formation of compact localized states and the emergence of flat bands. The CLS of an ABF lattice form an orthogonal and complete set of the Hilbert space [39, 70]. The orthogonality and completeness of the CLS imply that there exist specific choices of the unit-cell representation that eliminate all the inter-cell hopping matrices, $H_j^s = 0$. This type of representations is called *Semi-Detangled* (SD), and the lattice in then formed by decoupled unit cells [71]. An all-band-flat lattice therefore can be recast from the ND representation into the SD representation (and *vice versa*) via local unitary operators $\boldsymbol{U}$ – *i.e.* operating between neighboring unit-cells [39].

We now use this entangling process via local unitary operator to construct ABF lattices with broken TRS. The construction scheme begins from the SD representation of an ABF. First, we choose plaquettes (*i.e.,* a closed loop of M sites that does not intersect itself) threaded with a magnetic field as detangled unit cells — hence breaking TRS. We switch to an ND representation through the rotations $\boldsymbol{U}$ that do not alter TRS status of the lattice. The rotation $\boldsymbol{U}$ is formed of local unitary transformations $U \in \mathrm{SU}(r)$ involving r sites of two or more neighboring plaquettes. Such procedure however, in general produces highly intricate hoppings which may have limited physical applicability, although mathematically sound. To counter this and generate the ABFs without deforming the plaquettes with threaded magnetic fields, we attach auxiliary sites to the plaquettes (a.k.a appendices) and apply the unitaries $\boldsymbol{U}$ to entangle those neighboring appendices.

We illustrate our scheme with a one dimensional lattice with the smallest possible number of Bloch bands. We progress subsequently to more complex cases.

A. A simple case

Let us exemplify our construction scheme through the simplest case: a one-dimensional ABF lattice built from disjoint triangular plaquettes. We break TRS in each plaquette by threading them with a magnetic field of flux ϕ [72]. The corresponding matrix H_0 in Eq. (1) reads

$$H_{0,\Delta} = \begin{pmatrix} 0 & e^{\frac{\mathrm{i}\phi}{3}} & e^{-\frac{\mathrm{i}\phi}{3}} \\ e^{-\frac{\mathrm{i}\phi}{3}} & 0 & e^{\frac{\mathrm{i}\phi}{3}} \\ e^{\frac{\mathrm{i}\phi}{3}} & e^{-\frac{\mathrm{i}\phi}{3}} & 0 \end{pmatrix} \tag{3}$$

This plaquette forms the unit-cell of the lattice Hamiltonian H of Eq. (1) and the resulting structure corresponds to a semi-detangled (SD) ABF lattice, Fig. 1(a). A triangular plaquette in Fig. 1(a) has $\nu = 3$ flat bands (eigenstates of H_0 (3))

$$E_1 = 2\cos\frac{\phi}{3}, \qquad E_{2,3} = -\cos\frac{\phi}{3} \pm \sqrt{3}\sin\frac{\phi}{3} \tag{4}$$

These flat band eigenstates are completely localized within each plaquette yet carry a non-zero probability current due to the enclosed magnetic flux. We can compute this probability current $\mathcal{J}_{\boldsymbol{m};\mu,\eta}$ induced by a wavefunction ψ between two adjacent lattice sites μ and η of neighboring unit-cell at $\mathbf{m}$ and $\mathbf{m}'$, respectively, using [73]

$$\mathcal{J}_{\boldsymbol{m},\mu;\boldsymbol{m'},\eta} = \mathrm{i}\left\{\psi^*_{\boldsymbol{m},\mu}[H]_{\mu,\eta}\psi_{\boldsymbol{m'},\eta} - \psi^*_{\boldsymbol{m'},\eta}[H^\dagger]_{\mu,\eta}\psi_{\boldsymbol{m},\mu}\right\}, \tag{5}$$

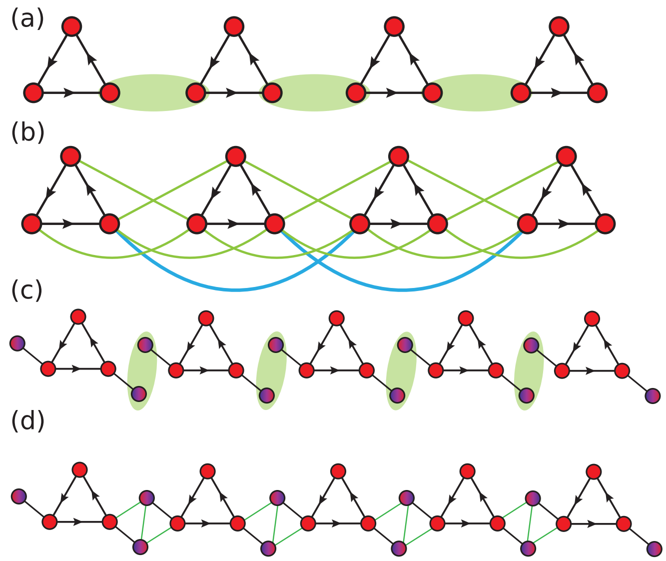

FIG. 1. (a) 1D lattice formed by stacking unit cells, that are triangles threaded by a flux ϕ. Green shadings mark the sites to which local unitary operation is applied (b) Resulting lattice after the entangling rotations. (c,d) Same as (a,b) but for triangular plaquettes with auxiliary sites.

where $\psi_{\boldsymbol{m},\nu}$ is the ν^{th} site component of the wavefunction of unit-cell at $\mathbf{m}$. Here H is the intra-cell hopping matrix H_0 if $\boldsymbol{m} = \boldsymbol{m'}$, else it is the inter-cell hopping matrix H_j^s between neighboring unit-cells at $\boldsymbol{m}$ and $\boldsymbol{m'}$ in the $\vec{a}_j$ direction. For instance, the eigenstates associated to $E_1 = 2\cos\frac{\phi}{3}$ has equal amplitudes in all three sites $\psi_{m,\mu} = \frac{1}{\sqrt{3}}$ for $\mu = 1,2,3$, which implies $\mathcal{J}_{m,\mu,m,\eta} = \frac{2}{3}\sin\frac{\phi}{3}$ in each bond. The total current in a flux-threaded plaquette m corresponding to a CLS is computed via the sum $\mathcal{J} = \sum_\mu \mathcal{J}_{m,\mu,m,\mu+1}$ using Eq. (5). In the lattice in Fig. 1(a), the total current corresponding to the CLS associated to $E_1 = 2\cos\frac{\phi}{3}$ is then $\mathcal{J} = 2\sin\frac{\phi}{3}$.

To transition from SD to ND representation without breaking the TRS nature of the Hamiltonian H, (see Appendix A for details), we design a suitable unitary transformation $\boldsymbol{U}$ formed of rotations $U \in \mathrm{SU}(2)$

$$U = \begin{pmatrix} \cos\theta & \sin\theta \\ -\sin\theta & \cos\theta \end{pmatrix} \tag{6}$$

for an angle $\theta \in [0, 2\pi]$. This transformation $\boldsymbol{U}$ acts on pairs of sites from neighboring triangular plaquettes — as shown in Fig. 1(a) with green shading (see Appendix B 1 for details on the construction of $\boldsymbol{U}$). The resulting ND lattice is shown in Fig. 1(b). The intra-cell matrix of its Hamiltonian H' is

$$H'_{0,\Delta} = \begin{pmatrix} 0 & e^{\frac{\mathrm{i}\phi}{3}}\cos\theta & e^{-\frac{\mathrm{i}\phi}{3}}\cos\theta \\ e^{-\frac{\mathrm{i}\phi}{3}}\cos\theta & 0 & e^{\frac{\mathrm{i}\phi}{3}}\cos\theta \\ e^{\frac{\mathrm{i}\phi}{3}}\cos\theta & e^{-\frac{\mathrm{i}\phi}{3}}\cos\theta & 0 \end{pmatrix} \tag{7}$$

while the nearest-neighbor hopping matrix is

$$H^{1\,\prime}_{1,\Delta} = \begin{pmatrix} 0 & 0 & -e^{\frac{\mathrm{i}\phi}{3}}\sin\theta \\ e^{\frac{\mathrm{i}\phi}{3}}\sin\theta & \frac{1}{2}e^{-\frac{\mathrm{i}\phi}{3}}\sin 2\theta & 0 \\ 0 & 0 & -e^{-\frac{\mathrm{i}\phi}{3}}\sin\theta \end{pmatrix} \tag{8}$$

Additionally, this lattice has next-to-nearest neighbor hopping terms, which are encoded in the matrix

$$H^{2\,\prime}_{1,\Delta} = \begin{pmatrix} 0 & 0 & 0 \\ 0 & 0 & -e^{-\frac{\mathrm{i}\phi}{3}}\sin^2\theta \\ 0 & 0 & 0 \end{pmatrix} \tag{9}$$

In Fig. 1(b), the hopping terms encoded by these three matrices are denoted by bonds colored in black, green and blue, respectively.

This construction does produce a family of ABF lattices with broken TRS. However, the resulting inter-cell hoppings in general have complex topology, Fig. 1(b), deviating from the original objective of simple and intuitive lattices. To counter this, we embed each triangular plaquette in Fig. 1(a) in an extended unit cell by appending two auxiliary sites, as shown in Fig. 1(c). This extends the unit cell to five sites, whose intra-cell matrix H_0 reads

$$H_{0,\blacktriangle} = \begin{pmatrix} 0 & e^{\frac{\mathrm{i}\phi}{3}} & e^{-\frac{\mathrm{i}\phi}{3}} & 1 & 0 \\ e^{-\frac{\mathrm{i}\phi}{3}} & 0 & e^{\frac{\mathrm{i}\phi}{3}} & 0 & 1 \\ e^{\frac{\mathrm{i}\phi}{3}} & e^{-\frac{\mathrm{i}\phi}{3}} & 0 & 0 & 0 \\ 1 & 0 & 0 & 1 & 0 \\ 0 & 1 & 0 & 0 & 1 \end{pmatrix} \tag{10}$$

Similar to the case of the triangular plaquette in Eq. (3), the five CLSs posses non-zero currents within the plaquette, which can be computed via Eq. (5).

A unitary transformation $\boldsymbol{U}$ that entangles this SD lattice, in this case involves the auxiliary sites of two adjacent plaquettes — as shown with green shaded areas of Fig. 1(c). The corresponding intra- and inter-cell matrices H_0 and H_1 of the ND Hamiltonian become

$$\begin{aligned} H'_{0,\blacktriangle} &= \begin{pmatrix} 0 & e^{\frac{\mathrm{i}\phi}{3}} & e^{-\frac{\mathrm{i}\phi}{3}} & \cos(\omega) & 0 \\ e^{-\frac{\mathrm{i}\phi}{3}} & 0 & e^{\frac{\mathrm{i}\phi}{3}} & 0 & 1 \\ e^{\frac{\mathrm{i}\phi}{3}} & e^{-\frac{\mathrm{i}\phi}{3}} & 0 & 0 & 0 \\ \cos\omega & 0 & 0 & 1 & 0 \\ 0 & 1 & 0 & 0 & 1 \end{pmatrix} \\ H'_{1,\blacktriangle} &= \begin{pmatrix} 0 & 0 & 0 & 0 & -\sin\omega \\ 0 & 0 & 0 & 0 & 0 \\ 0 & 0 & 0 & 0 & 0 \\ 0 & \sin\omega & 0 & 0 & 0 \\ 0 & 0 & 0 & 0 & 0 \end{pmatrix} \end{aligned} \tag{11}$$

With respect to the previous ND lattice shown in Fig. 1(b), the hopping terms that connect neighboring plaquettes are simplified to rhombii. Intuitively, these appendices induce "directions" along which the disconnected plaquettes are entangled, forming a lattice. This simplification of the hopping structure in the ND representation comes at the cost of the number of bands increasing from three to five, and subsequent increase of the dimensionality of Hilbert space. Nevertheless, the entangling process does not perturb the triangular plaquettes, nor the CLS components sitting therein. Hence, the local currents $\mathcal{J}_{\mu,\eta}$ are untouched. These CLSs, which exhibit localized probability current due to magnetic flux within the plaquette act as *vortices* in the lattice. Consequently, TRS breaking induces a macroscopically degenerate family of linear vortex states.

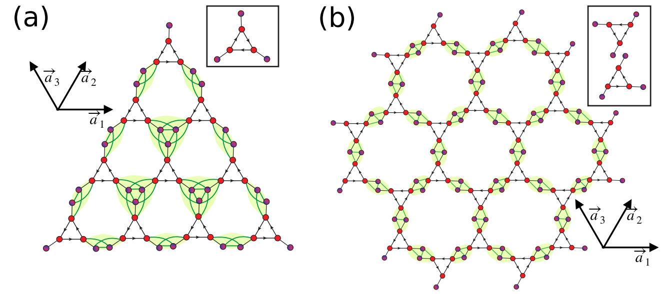

FIG. 2. (a) 2D ABF lattice with a different tiling of triangular unit cells (inset). In both cases hoppings induced by local unitary transformation are shown by green bonds. (b) 2D ABF lattice generated from hexagonal tiling of triangular unit cells threaded by a flux ϕ (inset). In both panels, $\vec{a}_1$ and $\vec{a}_2$ are the primitive translation vectors, with $\vec{a}_3 = \vec{a}_2 - \vec{a}_1$.

B. Two and three dimensional lattices

In one dimension, the construction scheme shown in Fig. 1 which starts from flux-threaded triangular plaquettes can be straightforwardly extended to larger plaquettes, *e.g.,* squares, pentagons, and beyond. The choices of the construction of the entangling unitary transformations $\boldsymbol{U}$ and the placement of auxiliary sites create a wide variety of ABF lattices with broken time-reversal symmetry. In the previous section, our results also highlighted that reducing the complexity of the hopping profile of the lattice can be achieved by increasing the number of sites per unit cell (*i.e.* the number of flat bands). We now extend this construction scheme to higher dimensional lattices, where an additional choice in the construction is the arrangement of the primitive lattice translation vectors $\vec{a}_j$ in Eq. (1), *i.e.* the choice of the Bravais lattice.

To describe the construction in higher dimensions, as in the previous subsection, we use triangular plaquettes. In two dimensions, the basic unit cell is shown in the inset of Fig. 2(a), and it is formed by a flux-threaded three-sites loop with an appendix site attached at each corner. Its Hamiltonian matrix reads

$$H_{0,\blacktriangle} = \begin{pmatrix} 0 & e^{\frac{i\phi}{3}} & e^{-\frac{i\phi}{3}} & 1 & 0 & 0 \\ e^{-\frac{i\phi}{3}} & 0 & e^{\frac{i\phi}{3}} & 0 & 1 & 0 \\ e^{\frac{i\phi}{3}} & e^{-\frac{i\phi}{3}} & 0 & 0 & 0 & 1 \\ 1 & 0 & 0 & 1 & 0 & 0 \\ 0 & 1 & 0 & 0 & 1 & 0 \\ 0 & 0 & 1 & 0 & 0 & 1 \end{pmatrix} \tag{12}$$

These six-sites unit cells are periodically repeated along the primitive vectors $\vec{a}_1$ and $\vec{a}_2$ shown in Fig. 2(a), which form a $\frac{\pi}{3}$ angle. The SD lattice is then entangled by applying local unitary rotations from SU(3) involving groups of three neighboring auxiliary sites. This entangling procedure result in the green bonds shown in Fig. 2(a) that link the neighboring flux-threaded triangular plaquettes without altering the TRS breaking of the system, see Appendix B 2 for details. The resulting hopping network that links neighboring triangular plaquettes is again rather complex. To reduce the complexity and design physical lattices, we extend the six site unit cell to a twelve site unit cell by pairing two six site structures in Eq. (12) one on top of the other; as shown in the inset of Fig. 2(b). These extended unit cells are then periodically arranged along the same primitive vectors as in Fig. 2(a) so that only pairs of auxiliary sites will be entangled via SU(2) unitary rotations in Eq. (6). The bonds between the auxiliary sites created by entangling are shown in green. This construction simplifies the hopping geometry while preserving the flux-threaded plaquettes; hence, resulting in a twelve-band ABF lattice whose geometry resembles the two-dimensional pyrochlore structure.

In three dimensions, we extend the triangular plaquettes to tetrahedra, where each triangular face is threaded by a magnetic flux which ensures TRS breaking. To each vertex of each tetrahedron we append an auxiliary site. This results in an eight-site unit cell shown in Fig. 3(a) whose matrix extends Eqs. (10,12) to an eight-by-eight matrix. These unit cells are periodically arranged along the primitive lattice vectors $\vec{a}_1$,$\vec{a}_2$ and $\vec{a}_3$, and entangled using local SU(4) transformations acting on groups of neighboring auxiliary sites (yellow shaded regions in Fig. 3(a)). The resulting eight-band ABF lattice has a complex hopping structure that links the neighboring tetrahedra. This structure, obtained via a set of SU(4) unitary rotations, can again be simplified by increasing the number of bands. Consider the case of Fig. 3(b): here we extend the unit cell to contain 16 bands, and therefore require a combination of SU(2) (yellow shaded regions) and SU(8) (purple shaded regions) rotations to entangle the neighboring unit cells. These two and three dimensional cases, shown in Fig. 2 and Fig. 3, highlight that reduction in hopping complexity of a generated ABF typically comes at the cost of increasing the number of Bloch bands.

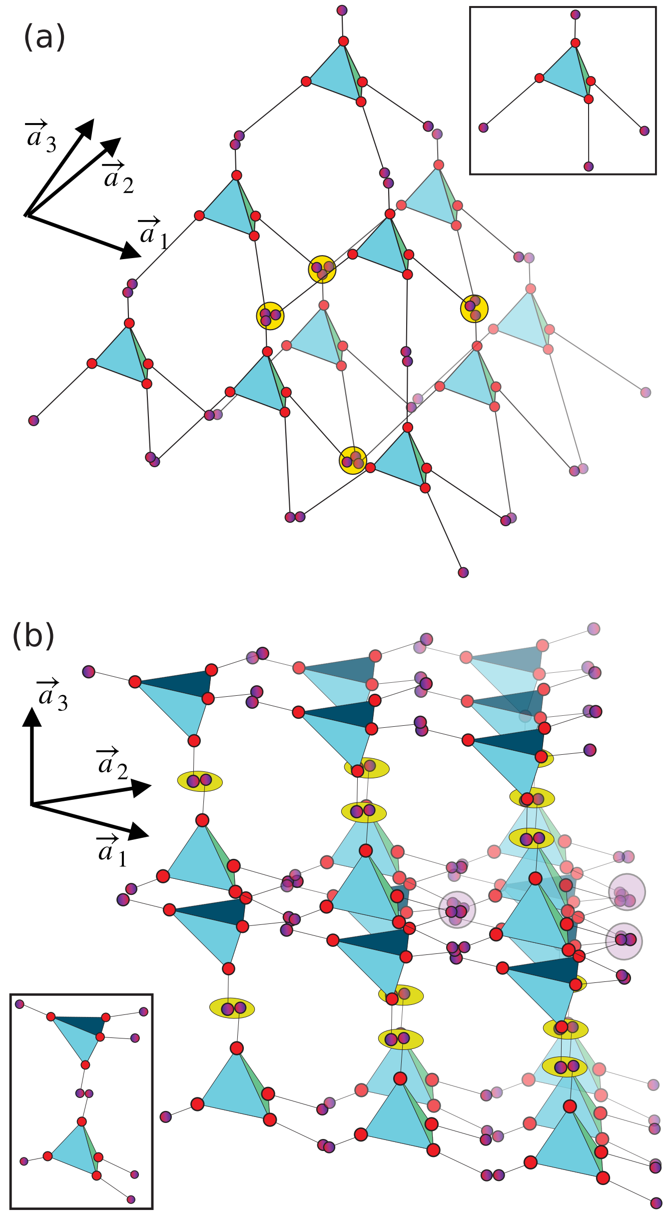

FIG. 3. (a) 3D ABF lattice generated from pyramid-like tiling of tetrahedral unit cells with appendices (shown in the inset). (b) a different tiling producing a 3D ABF network with 16-band and a tetrahedral unit cell with appendices (see inset). In both the panels, $\vec{a}_1, \vec{a}_2$ and $\vec{a}_3$ are the primitive translation vectors and the sites undergoing local unitary transformations are shown in shaded yellow and purple ellipses.

C. Currents in compact localized states

In this subsection, we focus on currents $\mathcal{J}$ which are induced on the CLS associated to the flat bands by the flux. These currents are obtained by summing all the local probability currents $\mathcal{J}_{\boldsymbol{m},\mu;\boldsymbol{m'},\eta}$ defined in Eq. (5). To discuss this, and to further present the construction of this class of ABF lattices, we consider the case of a flux-threaded square plaquette ($M = 4$) with four appen-

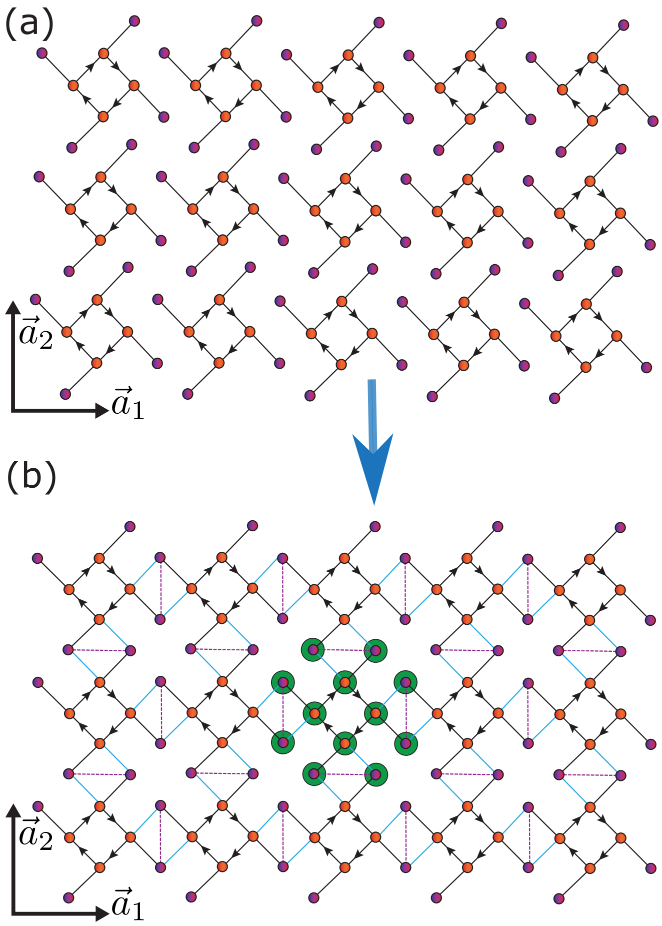

FIG. 4. (a) Two dimensional semi-detangled ABF lattice obtained by tiling augmented square unit-cells. With the shaded areas we indicate the sites chosen for the local unitary operations $\boldsymbol{U}$. The green and the pink colors denote the x and y direction in which the two rotations U_x and U_y which form $\boldsymbol{U}$ are applied. (b) Resulting non-detangled ABF lattice. With the green circles we show the location of CLS. In both the panels, $\vec{a}_1$ and $\vec{a}_2$ are the primitive translation vectors.

dices at each vertex. This results in an eight-site unit-cell whose matrix H_0 in the Hamiltonian H in Eq. (1) is

$$H_{0,\blacklozenge} = \begin{bmatrix} 0 & e^{\frac{i\phi}{4}} & 0 & e^{-\frac{i\phi}{4}} & 1 & 0 & 0 & 0 \\ e^{-\frac{i\phi}{4}} & 0 & e^{\frac{i\phi}{4}} & 0 & 0 & 1 & 0 & 0 \\ 0 & e^{-\frac{i\phi}{4}} & 0 & e^{\frac{i\phi}{4}} & 0 & 0 & 1 & 0 \\ e^{\frac{i\phi}{4}} & 0 & e^{-\frac{i\phi}{4}} & 0 & 0 & 0 & 0 & 1 \\ 1 & 0 & 0 & 0 & -1 & 0 & 0 & 0 \\ 0 & 1 & 0 & 0 & 0 & 1 & 0 & 0 \\ 0 & 0 & 1 & 0 & 0 & 0 & 1 & 0 \\ 0 & 0 & 0 & 1 & 0 & 0 & 0 & -1 \end{bmatrix}. \tag{13}$$

We arrange these unit cells in two-dimensions following orthogonal primitive lattice vectors $\vec{a}_1$ and $\vec{a}_2$, which result in the SD lattice shown in Fig. 4(a). We entangle the auxiliary sites of the neighboring unit cells (highlighted area in pink and green in Fig. 4) via SU(2) unitary rotations U_x and U_y in the x and y directions. In principle, these two local unitary rotations can be different. For simplicity, considering the entangling rotation by ω in both direction, the resulting intra-cell hopping matrix $H'_{0,\blacklozenge}$ is

$$H'_{0,\blacklozenge} = \begin{bmatrix} 0 & e^{\frac{i\phi}{4}} & 0 & e^{-\frac{i\phi}{4}} & c & 0 & 0 & 0 \\ e^{-\frac{i\phi}{4}} & 0 & e^{\frac{i\phi}{4}} & 0 & 0 & c & 0 & 0 \\ 0 & e^{-\frac{i\phi}{4}} & 0 & e^{\frac{i\phi}{4}} & 0 & 0 & c & 0 \\ e^{\frac{i\phi}{4}} & 0 & e^{-\frac{i\phi}{4}} & 0 & 0 & 0 & 0 & c \\ c & 0 & 0 & 0 & -C_\omega & 0 & 0 & 0 \\ 0 & c & 0 & 0 & 0 & C_\omega & 0 & 0 \\ 0 & 0 & c & 0 & 0 & 0 & C_\omega & 0 \\ 0 & 0 & 0 & c & 0 & 0 & 0 & -C_\omega \end{bmatrix}, \tag{14}$$

while the inter-cell hopping matrices $H'_{x,\blacklozenge}$, and $H'_{y,\blacklozenge}$ are

$$H'_{x,\blacklozenge} = \begin{bmatrix} 0&0&0&0&0&0&-s&0 \\ 0&0&0&0&0&0&0&0 \\ 0&0&0&0&0&0&0&0 \\ 0&0&0&0&0&0&0&0 \\ 0&0&s&0&0&0&S_\omega&0 \\ 0&0&0&0&0&0&0&0 \\ 0&0&0&0&0&0&0&0 \\ 0&0&0&0&0&0&0&0 \end{bmatrix}, H'_{y,\blacklozenge} = \begin{bmatrix} 0&0&0&0&0&0&0&0 \\ 0&0&0&0&0&0&0&-s \\ 0&0&0&0&0&0&0&0 \\ 0&0&0&0&0&0&0&0 \\ 0&0&0&0&0&0&0&0 \\ 0&0&0&s&0&0&0&-S_\omega \\ 0&0&0&0&0&0&0&0 \\ 0&0&0&0&0&0&0&0 \end{bmatrix} \tag{15}$$

where $C_\omega = \cos(2\omega)$, $S_\omega \equiv \sin(2\omega)$, $c = \cos(\omega)$ and $s = \sin(\omega)$. The resulting ND ABF lattice is shown in Fig. 4(b) corresponding to a family of two dimensional eight-bands ABF lattices with broken TRS. Each square plaquette which lies in the center of a unit cell is threaded with a magnetic field of flux ϕ. In Fig. 4(b) the green shaded regions show the sites of the eight compact localized states of the system.

In Fig. 5(a), we show an example of one of the eight CLS at $E = -1.74$ of the non-detangle ABF lattice obtained for $\omega = \pi/4$ and $\phi = 2$ in Eqs. (14,15). The amplitudes of the CLS are shown with bright colors, the current in the plaquette is shown along with the associated colorbar. The value of the current in the plaquette matches the corresponding value for the given parameters of Fig. 5(b). In Fig. 5(b) we plot the probability currents $\mathcal{J}$ of all eight orthogonal CLSs as function of the flux ϕ for $\omega = \pi/4$. These values are obtained by summing the local probability currents $\mathcal{J}_{\mu;\eta}$ defined in Eq. (5) in the flux-threaded square plaquette highlighted in blue in the inset of Fig. 5(b). All the currents $\mathcal{J}$ are non-zero, except for $\phi = 0, \pm\pi$ where time-reversal symmetry is restored in the lattice.

IV. GENERIC FLAT BAND LATTICES WITH BROKEN TIME REVERSAL SYMMETRY

In this section, we focus on constructing Hamiltonian lattices H in Eq. (1) with broken time-reversal symmetry featuring coexisting dispersive and flat bands. In other words, only a subset of the Bloch bands is independent of momentum $\mathbf{k}$ over the entire Brillouin zone, $E_\mu(\mathbf{k}) = \text{const}$ for $1 \le \mu \le \ell < \nu$. In this case however, differently from the ABF lattices discussed in the previous section, the CLS of a flat band can either form an orthogonal complete set, or form a non-orthogonal set [30]. On the one hand, orthogonal CLS sit within single unit cells of the flat band lattices, and they can be detangled from the remaining dispersive states via local unitary rotations $\boldsymbol{U}$ [31]. On the other hand, non-orthogonal CLS

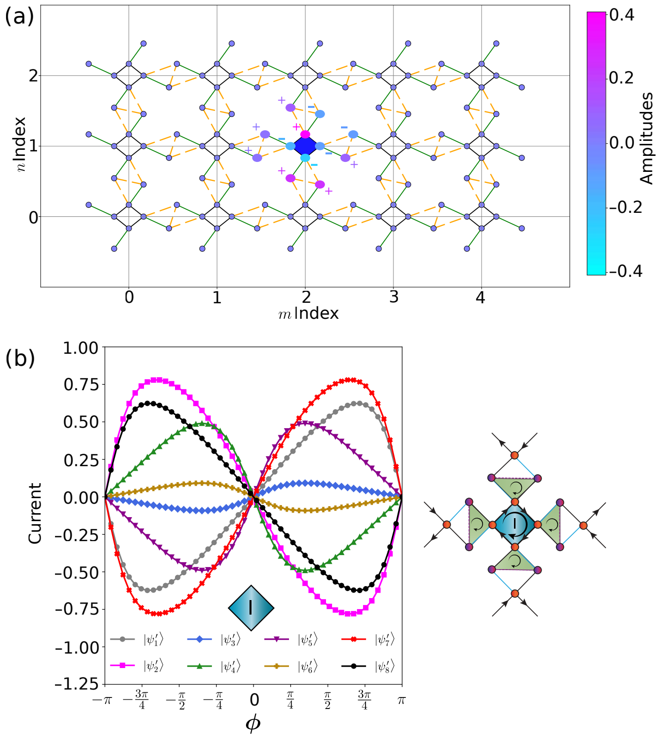

FIG. 5. (a) CLS amplitude shown in bright colors, whose intensities are encoded in the right colorbar. The CLS sites are displayed as larger markers, and the signs of their amplitudes are explicitly indicated for clarity. The blue shaded region indicates where the current circulates. (b) Probability current as a function of the flux ϕ for the eight different CLSs. In the lower right corner, we indicate the plaquettes where the current distribution is evaluated. On the right, it is indicated the plaquette labeled I where the current distribution is evaluated.

span over two or more unit cells, and they cannot be all detangled from the dispersive states via local unitary rotations [74]. In the following therefore, we treat the cases of orthogonal and non-orthogonal CLS separately.

A. Orthogonal CLS

Let us start with flat band lattices supporting orthogonal CLS. In the case, analogously to Sec. III, the construction scheme of flat band lattices with broken TRS relies on unitary rotations $\boldsymbol{U}$ that entangle disconnected flat band states into a dispersive lattice [31]. The scheme begins by first arranging flux-threaded plaquettes adjacently to a dispersive lattice. The total number of bands therefore is $M+\nu_d$, where M is the size of the plaquette, while ν_d is the number of dispersive bands. We then apply a unitary transformation $\boldsymbol{U}$ formed of local rotations U that entangle each plaquette with one unit-cell of the dispersive lattice [31]. This generally results in a complex lattices, which again can be simplified by attaching auxiliary sites to each plaquette.

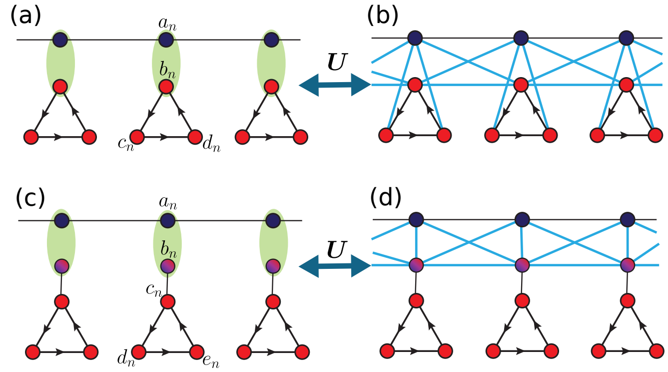

FIG. 6. (a) 1D lattice formed by disconnected flux-threaded triangular plaquetttes adjacent to a one-dimensional dispersive lattice. Orange shadings mark the sites to which local unitary operation is applied, while the blue shadings indicate the flux-threaded plaquettes (b) Resulting lattice after the entangling rotations. (c,d) Same as (a,b) for triangular plaquettes with auxiliary sites.

We shown an example in Fig. 6(a), which follows the simplest case in Sec. III A. In this case, we consider flux-threaded triangular plaquettes in Eq. (3), shaded in blue color, which we arranged adjacently to a one dimensional dispersive chain. The intra-cell and inter-cell matrices H_0 and H_1 of this lattice in the detangled representation are

$$H_0 = \begin{pmatrix} 0 & 0 & 0 & 0 \\ 0 & 0 & e^{\mathrm{i}\frac{\phi}{3}} & e^{-\mathrm{i}\frac{\phi}{3}} \\ 0 & e^{-\mathrm{i}\frac{\phi}{3}} & 0 & e^{\mathrm{i}\frac{\phi}{3}} \\ 0 & e^{\mathrm{i}\frac{\phi}{3}} & e^{-\mathrm{i}\frac{\phi}{3}} & 0 \end{pmatrix} \quad H_1 = \begin{pmatrix} 1 & 0 & 0 & 0 \\ 0 & 0 & 0 & 0 \\ 0 & 0 & 0 & 0 \\ 0 & 0 & 0 & 0 \end{pmatrix} \tag{16}$$

We then design a unitary transformation $\boldsymbol{U}$ formed by local rotations $U \in \mathrm{SU}(2)$ in Eq. (6) defined between pairs of sites, as highlighted with green shared areas. This yields an entangled lattice with four bands — three of which are flat whose values are in Eq. (4), while the fourth one is dispersive at $E(k) = 2\cos k$. The lattice is shown in Fig. 6(b), whose matrices are

$$H_0 = \begin{pmatrix} 0 & 0 & e^{\mathrm{i}\frac{\phi}{3}}\sin\theta & e^{-\mathrm{i}\frac{\phi}{3}}\sin\theta \\ 0 & 0 & e^{\mathrm{i}\frac{\phi}{3}}\cos\theta & e^{-\mathrm{i}\frac{\phi}{3}} \\ e^{-\mathrm{i}\frac{\phi}{3}}\sin\theta & e^{-\mathrm{i}\frac{\phi}{3}}\cos\theta & 0 & e^{\mathrm{i}\frac{\phi}{3}} \\ e^{\mathrm{i}\frac{\phi}{3}}\sin\theta & e^{\mathrm{i}\frac{\phi}{3}}\cos\theta & e^{-\mathrm{i}\frac{\phi}{3}} & 0 \end{pmatrix}$$

$$H_1 = \begin{pmatrix} \cos^2\theta & -\cos\theta\sin\theta & 0 & 0 \\ -\cos\theta\sin\theta & \sin^2\theta & 0 & 0 \\ 0 & 0 & 0 & 0 \\ 0 & 0 & 0 & 0 \end{pmatrix} \tag{17}$$

The resulting intricate hopping profile of the generated lattice can be simplified, alike in Sec. III A, by extending each plaquette with an auxiliary site, as shown in Fig. 6(c). The matrices of the SD lattice with the augmented plaquettes are

$$H_0 = \begin{pmatrix} 0 & 0 & 0 & 0 & 0 \\ 0 & 0 & 1 & 0 & 0 \\ 0 & 1 & 0 & e^{\mathrm{i}\frac{\phi}{3}} & e^{-\mathrm{i}\frac{\phi}{3}} \\ 0 & 0 & e^{-\mathrm{i}\frac{\phi}{3}} & 0 & e^{\mathrm{i}\frac{\phi}{3}} \\ 0 & 0 & e^{\mathrm{i}\frac{\phi}{3}} & e^{-\mathrm{i}\frac{\phi}{3}} & 0 \end{pmatrix} \quad H_1 = \begin{pmatrix} 1 & 0 & 0 & 0 & 0 \\ 0 & 0 & 0 & 0 & 0 \\ 0 & 0 & 0 & 0 & 0 \\ 0 & 0 & 0 & 0 & 0 \\ 0 & 0 & 0 & 0 & 0 \end{pmatrix} \tag{18}$$

The entangling process between the dispersive chain and the auxiliary sites, highlighted with green shared areas within each unit-cell, yields the entangled lattice shown in Fig. 6(d), whose matrices are

$$H_0 = \begin{pmatrix} 0 & 0 & \sin\theta & 0 & 0 \\ 0 & 0 & \cos\theta & 0 & 0 \\ \sin\theta & \cos\theta & 0 & e^{\mathrm{i}\frac{\phi}{3}} & e^{-\mathrm{i}\frac{\phi}{3}} \\ 0 & 0 & e^{-\mathrm{i}\frac{\phi}{3}} & 0 & e^{\mathrm{i}\frac{\phi}{3}} \\ 0 & 0 & e^{\mathrm{i}\frac{\phi}{3}} & e^{-\mathrm{i}\frac{\phi}{3}} & 0 \end{pmatrix}$$
$$H_1 = \begin{pmatrix} \cos^2\theta & -\cos\theta\sin\theta & 0 & 0 & 0 \\ -\cos\theta\sin\theta & \sin^2\theta & 0 & 0 & 0 \\ 0 & 0 & 0 & 0 & 0 \\ 0 & 0 & 0 & 0 & 0 \\ 0 & 0 & 0 & 0 & 0 \end{pmatrix} \tag{19}$$

In this case, the flux-threaded triangular plaquettes shaded in blue where the non-zero flux currents are located, remain unchanged. Let us observe that this construction can not only be extended by increasing the plaquette size and changing the unitary rotations $\boldsymbol{U}$, but also by considering a different dispersive lattice set adjacently to the plaquettes.

B. Non-orthogonal CLS

Flat bands supporting non-orthogonal CLS with broken TRS and non-zero flux are harder to come by, since systematic construction schemes are harder to come by (see however the recently developed approach using Bloch compact localized states [30]). Indeed, unlike the previous ABF case discussed in Sec. III and orthogonal FB in Sec. IV, no local unitary rotations $\boldsymbol{U}$ can be exploited. However, this kind of flat bands exist and they can be constructed explicitly.

An example is displayed in Fig. 7(a) and it is defined by intracell and intercell matrices

$$H_0 = \begin{pmatrix} 0 & 0 & e^{\mathrm{i}\phi} \\ 0 & 0 & e^{-\mathrm{i}\phi} \\ e^{-\mathrm{i}\phi} & e^{\mathrm{i}\phi} & 0 \end{pmatrix}, \quad H_1 = \begin{pmatrix} e^{-\mathrm{i}\phi} & 0 & 1 \\ 0 & e^{\mathrm{i}\phi} & 1 \\ 0 & 0 & 0 \end{pmatrix} \tag{20}$$

This lattice, as detailed in Appendix C, is obtained by breaking the chiral symmetry of a diamond chain with the horizontal hopping within the a and the c sublattices. Then, the lattice's plaquettes are thread with carefully oriented magnetic fields, whose flux is controlled by ϕ. This procedure renders one flat band at $E = -2$

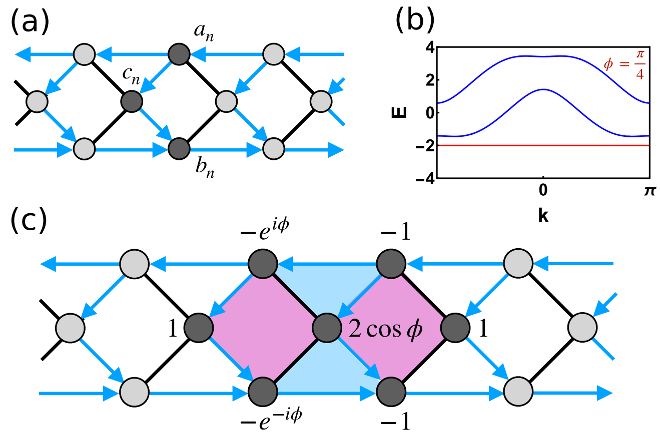

FIG. 7. (a) One dimensional flat band lattice with four-site flux-threaded plaquette. (b) Band structure for flux $\phi = \frac{\pi}{4}$. The $E = -2$ flat band is colored in red, while the two dispersive bands are colored in blue. (c) CLS as function of the flux ϕ. The blue shaded regions indicate where the current circulates.

and two dispersive bands $E_{2,3} = 1 + 2\cos\phi\cos k \pm (1 - \cos(2k) - 2\cos(2\phi)\sin^2 k)^{\frac{1}{2}}$ — shown in Fig. 7(b) for $\phi = \frac{\pi}{4}$. The ϕ-dependent CLS associated to the flat band is shown in Fig. 7(c). The flux induces currents circulating within the plaquettes shaded in blue and pink colors, which respectively $\mathcal{J} = -6\sin 2\phi$ and $\mathcal{J} = 4\sin 2\phi$. The total current in the CLS is given by double the sum of these two currents and is non-zero.

C. Chiral flat band lattices with broken TRS

An important class of flat-band systems is formed by chiral FBs, where the existence of the flat band is guaranteed by the chiral (sublattice) symmetry of the lattice. This class has been explored extensively in Refs. [35, 36, 75–77]. In the paradigmatic example of Vidal *et al.* [35], complex hoppings on the diamond lattice generate Hamiltonians in which TRS is broken. Furthermore, the CLS at the flat-band energy is non-orthogonal for a general flux threaded through the lattice Khomeriki and Flach [76].

In such systems, the CLS has non-zero amplitude only on the majority sublattices (a_n, b_n) and fails to occupy all sites of any flux-threaded plaquette. As a result, no gauge-invariant current loop can be formed, and each plaquette contributes zero net current. In the remaining cases where the CLS does occupy all sites of a flux-threaded polygon, either (i) its amplitudes are entirely real—yielding no current; or (ii) the corresponding flux configuration preserves TRS, placing it outside the scope of the present work.

Thus, chiral flat bands with broken TRS differ fundamentally from both the ABF constructions and the more general flat-band architectures developed here: they cannot support compact current vortices.

V. DISCUSSION AND CONCLUSION

We have provided a protocol of generating all-bands-flat lattices with broken time reversal symmetry. We introduced the TRS breaking by threading magnetic flux through polygonal plaquettes (M sites). Although we focused our attention on triangle and square plaquettes, our protocol can be trivially extended to any polygonal plaquettes. Besides, we show that just selecting the plaquettes and using entangling unitaries, we can (a) preserve the broken time reversal symmetry, and (b) transform the semi-detangled lattice to non-detangled lattice; we end up with ABF lattices with non-trivial hopping and complicated network. Therefore, we introduce appendices to each of the vertices of the the plaquettes which allow us to braid an ABF lattice in 1D (Fig. 1), 2D (Figs. 2, 4), and 3D (Fig. 3) as well as leave the flux threaded plaquettes unspoiled. However, the introduction of appendices increase the number of bands twofold, *i.e.,* $2M$, with the benefit of easier extendability to higher dimensions. We can stack $L = 2, 3, ...$ augmented plaquettes allowing us to reduce the complex hopping junctions to rhombic hopping. This results in families of physically relevant ABF lattices with broken TRS with $2ML$ bands. The CLS in these systems occupy the initial plaquette and auxiliary sites, along with the entangled sites from neighboring unit cells involved in the unitary transformation $\boldsymbol{U}$. The CLS components residing in the flux-threaded plaquettes generate nonzero local currents, effectively behaving as localized lattice vortices.

We further show that our construction is also implementable to systems with flat-band in presence of dispersive bands. We consider the cases of orthogonal (Fig. 6), and non-orthogonal (Fig. 7) CLSs. We find our broken TRS systems contain localized circulation, however, unlike ABF or orthogonal cases, the non-orthogonal case has current in all the plaquettes as seen from the diamond lattice(Fig. 7(c)).

Our work opens up the possibility of studying localized currents in otherwise dispersionless lattice. Since these currents are dependent on the strength of the flux threaded through the plaquettes, it allows tunability, which can be of interest to the experimentalists of the subject. It can be shown, if the boundary conditions are disturbed, *i.e.,* edges are cut in a particular direction, *e.g.,* x-direction of the lattice in Fig. 4, we can get extended edge states. Unlike conventional topological edge states, which arise due to nontrivial bulk topology, the edge-localized modes observed here emerge as a result of structural modifications to an inherently dispersionless bulk. While the models studied here do not exhibit nontrivial Chern numbers, future work could explore whether additional topological features can emerge under different symmetry-breaking conditions.

ACKNOWLEDGMENT

RKR, AA, and SF acknowledge the support by the Institute for Basic Science in Korea (IBS-R024-D1). CD acknowledges the support the PNRR MUR project CN 00000013-ICSC. We thank Tilen Čadež, Dung Xuan Nguyen, and Yeongjun Kim for valuable discussions.

Appendix A: TRS versus unitary transformations

We consider a unitary operator $\boldsymbol{U} \in \mathcal{H}$ such that

$$H' := \boldsymbol{U} H \boldsymbol{U}^\dagger. \tag{A1}$$

Using the definition in Eq. (2) in the main text, we want to explore the conditions which will lead to H' be TRS, *i.e.,*

$$\mathcal{T} H' \mathcal{T}^{-1} = H'. \tag{A2}$$

Let us revisit the properties of anti-unitary transformations. Consider the following lemma —

Lemma 1. *Let $\mathcal{T}$ be an anti-unitary operator and A a bounded linear operator on $\mathcal{H}$. Then for any $|\phi\rangle, |\psi\rangle \in \mathcal{H}$,*

$$\langle \mathcal{T}\psi | \mathcal{T} A \mathcal{T}^{-1} | \mathcal{T}\phi \rangle = \left(\langle \phi | A | \psi \rangle \right)^*. \tag{A3}$$

Proof. Let $A' = \mathcal{T} A \mathcal{T}^{-1}$, then,

$$\langle \mathcal{T}\psi | A' | \mathcal{T}\phi \rangle = \langle \mathcal{T}\psi | \mathcal{T} A | \phi \rangle = \left(\langle \phi | A | \psi \rangle \right)^*, \tag{A4}$$

where in the last step we have used the anti-linearity and anti-unitarity properties of $\mathcal{T}$. □

From this lemma, we note the following:

$$\left(\mathcal{T} A \mathcal{T}^{-1} \right)^\dagger = \mathcal{T} A^\dagger \mathcal{T}^{-1}. \tag{A5}$$

We now state the main result of this appendix.

Theorem 1. *Let H be TRS, i.e., Eq. (2) holds, and define H' via Eq. (A1). Then H' is TRS if and only if*

$$[H, \mathcal{W}] = 0, \quad \mathcal{W} := \boldsymbol{U}^\dagger (\mathcal{T} \boldsymbol{U} \mathcal{T}^{-1}). \tag{A6}$$

Proof. Considering H with TRS, we write:

$$\begin{aligned} \mathcal{T} H' \mathcal{T}^{-1} &= \mathcal{T} (\boldsymbol{U} H \boldsymbol{U}^\dagger) \mathcal{T}^{-1} \\ &= (\mathcal{T} \boldsymbol{U} \mathcal{T}^{-1})(\mathcal{T} H \mathcal{T}^{-1})(\mathcal{T} \boldsymbol{U}^\dagger \mathcal{T}^{-1}) \\ &= (\mathcal{T} \boldsymbol{U} \mathcal{T}^{-1}) H (\mathcal{T} \boldsymbol{U} \mathcal{T}^{-1})^\dagger. \end{aligned} \tag{A7}$$

Thus, $\mathcal{T} H' \mathcal{T}^{-1} = H'$ if and only if (using Eq. (A1) on the rhs)

$$(\mathcal{T} \boldsymbol{U} \mathcal{T}^{-1}) H (\mathcal{T} \boldsymbol{U} \mathcal{T}^{-1})^\dagger = \boldsymbol{U} H \boldsymbol{U}^\dagger. \tag{A8}$$

Now, we define $\mathcal{W} := \boldsymbol{U}^\dagger(\mathcal{T}\boldsymbol{U}\mathcal{T}^{-1})$. Using this we can write Eq. (A8) as

$$\begin{aligned} \mathcal{W}H\mathcal{W}^\dagger &= H, \\ \mathcal{W}H &= H\mathcal{W}, \end{aligned} \tag{A9}$$

which implies

$$[H, \mathcal{W}] = 0. \tag{A10}$$

□

Corollary 1. *It follows from Theorem 1, a given unitary transformation $\boldsymbol{U}$ preserves the TRS of Hamiltonian H if it is itself TRS preserving,* i.e.,

$$\mathcal{T}\boldsymbol{U}\mathcal{T}^{-1} = \boldsymbol{U}. \tag{A11}$$

Proof. Follows from the main result of Theorem 1, Eq. (A6). The commutation is trivially satisfied if $\mathcal{W} = \mathrm{I}$ which immediately implies $\mathcal{T}\boldsymbol{U}\mathcal{T}^{-1} = \boldsymbol{U}$. □

1. Spinless Case and orthogonal transformations

For spinless systems, the time-reversal operator is simply complex conjugation: $\mathcal{T} = K$. In this case,

$$\mathcal{T}\boldsymbol{U}\mathcal{T}^{-1} = \mathcal{K}\boldsymbol{U}\mathcal{K} = \boldsymbol{U}^*,$$

so the condition (A11) becomes:

$$\boldsymbol{U} = \boldsymbol{U}^*, \tag{A12}$$

implying $\boldsymbol{U}$ to be a real unitary matrix, i.e. orthogonal matrix. Therefore, in spinless systems, TRS is preserved under orthogonal transformations. The overall conclusion is that time-reversal symmetry (TRS) is unaffected by orthogonal transformations.

Appendix B: Construction of the unitaries

We provide a general protocol for the construction of unitaries that introduce local rotations between the sites of different unit cells. We consider the local operations between two-sites and three-sites which can be extended to higher number of such sites.

1. Between two sites

Since the local operations only introduce rotation between two sites (of neighboring unit-cells), we consider an element of SU(2):

$$U = \begin{pmatrix} z & w \\ -w^* & z^* \end{pmatrix} \tag{B1}$$

parametrize by two complex numbers z and w such that $|z|^2 + |w|^2 = 1$. We construct $\boldsymbol{U}_v$ along the v-direction following a systematic protocol. Consider a lattice with N_x unit cells in the x-direction and N_y unit cells in the y-direction, where each unit cell contains ν sites. We initiate $\boldsymbol{U}_v$ by setting it equal to the identity matrix of size $(\nu N_x N_y) \times (\nu N_x N_y)$.

1. For each pair of sites (i, j) located in adjacent unit cells $\langle \boldsymbol{\mu}, \boldsymbol{\mu}' \rangle$ along the v-direction:
   (a) Diagonal Elements:
   $$[\boldsymbol{U}_v]_{\boldsymbol{\mu},i;\boldsymbol{\mu},i} = [U]_{11}, \quad [\boldsymbol{U}_v]_{\boldsymbol{\mu}',j;\boldsymbol{\mu}',j} = [U]_{22}. \tag{B2}$$
   (b) Off-Diagonal Elements:
   $$[\boldsymbol{U}_v]_{\boldsymbol{\mu}',j;\boldsymbol{\mu},i} = [U]_{21}, \quad [\boldsymbol{U}_v]_{\boldsymbol{\mu},i;\boldsymbol{\mu}',j} = [U]_{12}. \tag{B3}$$
2. For periodic boundary conditions, we apply the same substitutions to unit-cell pairs at both ends along the v-direction to ensure continuity:
   (a) Diagonal Elements:
   $$[\boldsymbol{U}_v]_{\boldsymbol{\mu},i;\boldsymbol{\mu},i} = [U]_{11}, \quad [\boldsymbol{U}_v]_{\boldsymbol{\mu}',j;\boldsymbol{\mu}',j} = [U]_{22}. \tag{B4}$$
   (b) Off-Diagonal Elements:
   $$[\boldsymbol{U}_v]_{\boldsymbol{\mu}',j;\boldsymbol{\mu},i} = [U]_{21}, \quad [\boldsymbol{U}_v]_{\boldsymbol{\mu},i;\boldsymbol{\mu}',j} = [U]_{12}. \tag{B5}$$

The process is repeated for each direction v as follows:

1. For $v = x$-direction ($\boldsymbol{\mu} = m, n;\ \boldsymbol{\mu}' = m', n$):
   (a) Step 1 (Eqs. (B2) – (B3)) is repeated $N_x - 1$ times for each fixed $n = 1, \ldots, N_y$.
   (b) Step 2 (Eqs. (B4) – (B5)) is applied between unit cells at $m = 1$ and $m' = N_x$, ensuring periodicity ($\boldsymbol{\mu}' = N_x, n;\ \boldsymbol{\mu} = 1, n$).
2. For $v = y$-direction ($\boldsymbol{\mu} = m, n;\ \boldsymbol{\mu}' = m, n'$):
   (a) Step 1 (Eqs. (B2) – (B3)) is repeated $N_y - 1$ times for each fixed $m = 1, \ldots, N_x$.
   (b) Step 2 (Eqs. (B4) – (B5)) is applied between unit cells at $n = 1$ and $n' = N_y$, ensuring periodicity ($\boldsymbol{\mu}' = m, N_y;\ \boldsymbol{\mu} = m, 1$).

2. Between three sites

The local operations will be formed by an element of SU(3). However, there are 8 real parameters (α_i for $i = 1 \cdots 8$) that can explicitly describe SU(3), it can be written as follows. Using 3×3 Gell-Mann matrices [78] λ_i for $i = 1 \cdots 8$, the general unitary can be written as:

$$U = \exp\left(\mathrm{i} \sum_{i=1}^{8} \alpha_i \lambda_i\right). \tag{B6}$$

However, for the demonstration of our construction, we use a real SO(3) (subgroup of SU(3)) matrix, parametrized by three Euler angles (θ, ϕ, ψ) as:

$$U = \begin{bmatrix} cp\,ct\,cps - sp\,sps & -cp\,ct\,sps - sp\,cps & cp\,st \\ sp\,ct\,cps + cp\,sps & -sp\,ct\,sps + cp\,cps & sp\,st \\ -st\,cps & st\,sps & ct \end{bmatrix}, \tag{B7}$$

where we have used the shorthands of the form #1#2 where in #1 we place c for cos, s for sin; and in #2 p, t, ps for ϕ, θ, and ψ, respectively. Now that we have given an example of the kind of unitaries we need, let us look at how to construct $\boldsymbol{U}_v$. For sites i, j, and k of unit-cells $\langle \boldsymbol{\mu}, \boldsymbol{\mu}', \boldsymbol{\mu}'' \rangle$, we do the following,

1. Diagonal Elements:

$$\begin{aligned} &[\boldsymbol{U}_v]_{\boldsymbol{\mu},i;\boldsymbol{\mu},i} = [U]_{11}, \quad [\boldsymbol{U}_v]_{\boldsymbol{\mu}',j;\boldsymbol{\mu}',j} = [U]_{22}, \\ &[\boldsymbol{U}_v]_{\boldsymbol{\mu}'',k;\boldsymbol{\mu}'',k} = [U]_{33}. \end{aligned} \tag{B8}$$

2. Off-Diagonal Elements:

$$\begin{aligned} [\boldsymbol{U}_v]_{\boldsymbol{\mu},i;\boldsymbol{\mu}',j} &= [U]_{12}, \quad [\boldsymbol{U}_v]_{\boldsymbol{\mu},i;\boldsymbol{\mu}'',k} = [U]_{13}, \\ [\boldsymbol{U}_v]_{\boldsymbol{\mu}',j;\boldsymbol{\mu}'',k} &= [U]_{23}, \quad [\boldsymbol{U}_v]_{\boldsymbol{\mu}',j;\boldsymbol{\mu},i} = [U]_{21}, \\ [\boldsymbol{U}_v]_{\boldsymbol{\mu}'',k;\boldsymbol{\mu},i} &= [U]_{31}, \quad [\boldsymbol{U}_v]_{\boldsymbol{\mu}'',k;\boldsymbol{\mu}',j} = [U]_{32}. \end{aligned} \tag{B9}$$

For periodic boundary conditions, we apply the same substitutions to unit-cell pairs at both ends along the v-direction to ensure continuity:

1. Diagonal Elements:

$$\begin{aligned} &[\boldsymbol{U}_v]_{\boldsymbol{\mu},i;\boldsymbol{\mu},i} = [U]_{11}, \quad [\boldsymbol{U}_v]_{\boldsymbol{\mu}',j;\boldsymbol{\mu}',j} = [U]_{22}, \\ &[\boldsymbol{U}_v]_{\boldsymbol{\mu}'',k;\boldsymbol{\mu}'',k} = [U]_{33}. \end{aligned} \tag{B10}$$

2. Off-Diagonal Elements:

$$\begin{aligned} [\boldsymbol{U}_v]_{\boldsymbol{\mu},i;\boldsymbol{\mu}',j} &= [U]_{12}, \quad [\boldsymbol{U}_v]_{\boldsymbol{\mu},i;\boldsymbol{\mu}'',k} = [U]_{13}, \\ [\boldsymbol{U}_v]_{\boldsymbol{\mu}',j;\boldsymbol{\mu}'',k} &= [U]_{23}, \quad [\boldsymbol{U}_v]_{\boldsymbol{\mu}',j;\boldsymbol{\mu},i} = [U]_{21}, \\ [\boldsymbol{U}_v]_{\boldsymbol{\mu}'',k;\boldsymbol{\mu},i} &= [U]_{31}, \quad [\boldsymbol{U}_v]_{\boldsymbol{\mu}'',k;\boldsymbol{\mu}',j} = [U]_{32}. \end{aligned} \tag{B11}$$

Appendix C: Construction of non-orthogonal flat bands with broken time reversal symmetry

In this section, we detail the construction of the flat band lattice with non-orthogonal CLS and broken time-reversal.

The construction starts from a one-dimensional diamond chain shown in Fig. 8(a), whose intra-cell and intercell matrices are

$$H_0 = \begin{pmatrix} 0 & 0 & 1 \\ 0 & 0 & 1 \\ 1 & 1 & 0 \end{pmatrix} \qquad H_1 = \begin{pmatrix} 0 & 0 & 1 \\ 0 & 0 & 1 \\ 0 & 0 & 0 \end{pmatrix} \tag{C1}$$

This lattice is chiral [77], as it splits in a majority sublattice $\{a_n, b_n\}$ and a minority sublattice $\{c_n\}$ with different cardinality. This implies that one Bloch band

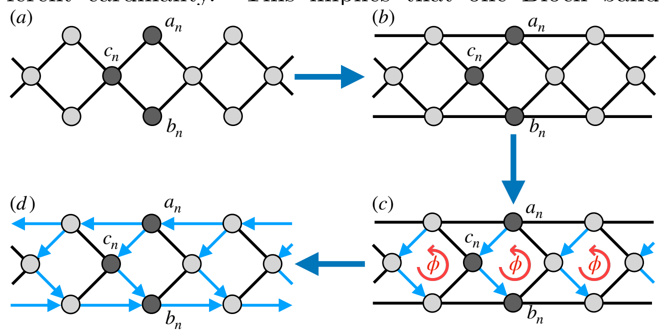

FIG. 8. (a) Three bands diamond chain. The unit-cell sites are colored in black. (b) Diamond chain with a chirality-breaking hopping connecting the nearest-neighboring a-sites. (c) Diamond chain with flux threading the central rhombic plaquettes. (d) Diamond chain with flux threading the central rhombic plaquettes and the upper and lower triangular plaquettes.

is flat at $E = 0$, while the two dispersive bands are $E_{1,2} = \pm 2\sqrt{1 + \cos k}$.

At first, we break the chirality of the lattice by adding horizontal hopping terms of the same strength of the rhombic hoppings, as shown in Fig. 8(b). This turns the three bands of the lattice to $E_1 = -2$, $E_2 = 2\cos k$ and $E_3 = 2(1 + \cos k)$.

We then thread the central rhombic plaquettes with a magnetic flux, as shown in Fig. 8(c). The intra-cell and intercell matrices in Eq. (C1) turn to

$$H_0 = \begin{pmatrix} 0 & 0 & e^{\mathrm{i}\phi} \\ 0 & 0 & e^{-\mathrm{i}\phi} \\ e^{-\mathrm{i}\phi} & e^{\mathrm{i}\phi} & 0 \end{pmatrix} \qquad H_1 = \begin{pmatrix} 1 & 0 & 1 \\ 0 & 1 & 1 \\ 0 & 0 & 0 \end{pmatrix} \tag{C2}$$

This however initially destroys the $E = -2$ flat bands, as the three bands are $E_1 = 2\cos k$ and $E_{2,3} = \cos k \pm \sqrt{4 + 4\cos k \cos\phi + \cos^2(k)}$.

At last, we turn the horizontal chirality-breaking hoppings complex, as shown in Fig. 8(d). The intra-cell and intercell matrices in Eq. (C2) turn to

$$H_0 = \begin{pmatrix} 0 & 0 & e^{\mathrm{i}\phi} \\ 0 & 0 & e^{-\mathrm{i}\phi} \\ e^{-\mathrm{i}\phi} & e^{\mathrm{i}\phi} & 0 \end{pmatrix} \qquad H_1 = \begin{pmatrix} e^{-\mathrm{i}\phi} & 0 & 1 \\ 0 & e^{\mathrm{i}\phi} & 1 \\ 0 & 0 & 0 \end{pmatrix} \tag{C3}$$

The three bands turn to $E_1 = -2$ and $E_{2,3} = 1 + 2\cos\phi\cos k \pm \sqrt{1 - \cos(2k) - 2\cos(2\phi)\sin^2 k}$.

[1] O. Derzhko, J. Richter, and M. Maksymenko, International Journal of Modern Physics B **29**, 1530007 (2015).
[2] D. Leykam, A. Andreanov, and S. Flach, Advances in Physics: X **3**, 1473052 (2018).
[3] D. Leykam and S. Flach, APL Photonics **3**, 070901 (2018).
[4] R. A. V. Poblete, Advances in Physics: X **6**, 1878057 (2021).
[5] J.-W. Rhim and B.-J. Yang, Advances in Physics: X **6**, 1901606 (2021).
[6] D. Leykam, AAPPS Bulletin **34**, 2 (2024).
[7] C. Danieli, A. Andreanov, D. Leykam, and S. Flach, Nanophotonics **13**, 3925 (2024).
[8] N. Read, Phys. Rev. B **95**, 115309 (2017).
[9] R. A. Vicencio, C. Cantillano, L. Morales-Inostroza, B. Real, C. Mejía-Cortés, S. Weimann, A. Szameit, and M. I. Molina, Phys. Rev. Lett. **114**, 245503 (2015).
[10] S. Mukherjee, A. Spracklen, D. Choudhury, N. Goldman, P. Öhberg, E. Andersson, and R. R. Thomson, Phys. Rev. Lett. **114**, 245504 (2015).
[11] S. Weimann, L. Morales-Inostroza, B. Real, C. Cantillano, A. Szameit, and R. A. Vicencio, Opt. Lett. **41**, 2414 (2016).
[12] S. Taie, H. Ozawa, T. Ichinose, T. Nishio, S. Nakajima, and Y. Takahashi, Science Advances **1**, e1500854 (2015).
[13] Y. He, R. Mao, H. Cai, J.-X. Zhang, Y. Li, L. Yuan, S.-Y. Zhu, and D.-W. Wang, Phys. Rev. Lett. **126**, 103601 (2021).
[14] C. Chase-Mayoral, L. Q. English, N. Lape, Y. Kim, S. Lee, A. Andreanov, S. Flach, and P. G. Kevrekidis, Phys. Rev. B **109**, 075430 (2024).
[15] N. Lape, S. Diubenkov, L. Q. English, P. G. Kevrekidis, A. Andreanov, Y. Kim, and S. Flach, Phys. Rev. B **112**, 184309 (2025), arXiv:2508.13571 [cond-mat.mes-hall].
[16] T.-X. Ma, Q.-S. Fan, C. Zhang, and Y.-S. Wang, Journal of Applied Physics **129**, 145104 (2021).
[17] Y.-X. Shen, Y.-G. Peng, P.-C. Cao, J. Li, and X.-F. Zhu, Phys. Rev. B **105**, 104102 (2022).
[18] B. Sutherland, Phys. Rev. B **34**, 5208 (1986).
[19] A. Mielke, J. Phys. A: Math. Gen. **24**, 3311 (1991).
[20] H. Tasaki, Phys. Rev. Lett. **69**, 1608 (1992).
[21] R. Dias and J. Gouveia, Sci. Rep. **5**, 16852 (2015).
[22] L. Morales-Inostroza and R. A. Vicencio, Physical Review A **94**, 043831 (2016).
[23] M. Röntgen, C. V. Morfonios, and P. Schmelcher, Physical Review B **97**, 035161 (2018).
[24] Y. Hwang, J.-W. Rhim, and B.-J. Yang, Phys. Rev. B **104**, 085144 (2021).
[25] D. Călugăru, A. Chew, L. Elcoro, Y. Xu, N. Regnault, Z.-D. Song, and B. A. Bernevig, Nature Physics **18**, 185 (2022).
[26] J.-W. Ryu, A. Andreanov, H. C. Park, and J.-H. Han, Journal of Physics A: Mathematical and Theoretical **57**, 495301 (2024), arXiv:2308.14997 [cond-mat.mes-hall].
[27] W. Maimaiti, A. Andreanov, H. C. Park, O. Gendelman, and S. Flach, Phys. Rev. B **95**, 115135 (2017).
[28] W. Maimaiti, S. Flach, and A. Andreanov, Phys. Rev. B **99**, 125129 (2019).
[29] W. Maimaiti, A. Andreanov, and S. Flach, Phys. Rev. B **103**, 165116 (2021).
[30] Y. Kim, S. Flach, and A. Andreanov, Real space decay of flat band projectors from compact localized states (2025), arXiv:2510.17258 [cond-mat.mes-hall].
[31] S. Flach, D. Leykam, J. D. Bodyfelt, P. Matthies, and A. S. Desyatnikov, Europhys. Lett. **105**, 30001 (2014).
[32] J.-W. Rhim and B.-J. Yang, Phys. Rev. B **99**, 045107 (2019).
[33] A. Graf and F. Piéchon, Phys. Rev. B **104**, 195128 (2021).
[34] H. Kim, C.-g. Oh, and J.-W. Rhim, Communications Physics **6**, 305 (2023), arXiv:2305.00448 [cond-mat.str-el].
[35] J. Vidal, R. Mosseri, and B. Douçot, Phys. Rev. Lett. **81**, 5888 (1998).
[36] J. Vidal, B. Douçot, R. Mosseri, and P. Butaud, Phys. Rev. Lett. **85**, 3906 (2000).
[37] G. Gligorić, P. P. Beličev, D. Leykam, and A. Maluckov, Phys. Rev. A **99**, 013826 (2019).
[38] M. Di Liberto, S. Mukherjee, and N. Goldman, Phys. Rev. A **100**, 043829 (2019).
[39] C. Danieli, A. Andreanov, T. Mithun, and S. Flach, Phys. Rev. B **104**, 085131 (2021).
[40] M. Tovmasyan, S. Peotta, L. Liang, P. Törmä, and S. D. Huber, Phys. Rev. B **98**, 134513 (2018).
[41] S. Tilleke, M. Daumann, and T. Dahm, Zeitschrift für Naturforschung A **75**, 393 (2020).
[42] C. Danieli, A. Andreanov, T. Mithun, and S. Flach, Phys. Rev. B **104**, 085132 (2021).
[43] O. Hart, G. De Tomasi, and C. Castelnovo, Phys. Rev. Research **2**, 043267 (2020).
[44] Y. Kuno, T. Mizoguchi, and Y. Hatsugai, Phys. Rev. B **102**, 241115 (2020).
[45] Y. Kuno, T. Mizoguchi, and Y. Hatsugai, Phys. Rev. B **104**, 085130 (2021).
[46] G. Pelegrí, S. Flannigan, and A. J. Daley, Phys. Rev. B **109**, 235412 (2024).
[47] C. Danieli, A. Andreanov, and S. Flach, Phys. Rev. B **102**, 041116 (2020).
[48] Y. Kuno, T. Orito, and I. Ichinose, New J. Phys. **22**, 013032 (2020).
[49] T. Orito, Y. Kuno, and I. Ichinose, Phys. Rev. B **103**, L060301 (2021).
[50] S. Mukherjee, M. Di Liberto, P. Öhberg, R. R. Thomson, and N. Goldman, Phys. Rev. Lett. **121**, 075502 (2018).
[51] M. Kremer, I. Petrides, E. Meyer, M. Heinrich, O. Zilberberg, and A. Szameit, Nat. Comm. **11**, 907 (2020).
[52] C. Jorg, G. Queraltó, M. Kremer, G. Pelegrí, J. Schulz, A. Szameit, G. von Freymann, J. Mompart, and V. Ahufinger, Light: Science & Applications **9**, 2047 (2020).
[53] G. Cáceres-Aravena, D. Guzmán-Silva, I. Salinas, and R. A. Vicencio, Phys. Rev. Lett. **128**, 256602 (2022).
[54] D. Roman-Cortes, M. Mazanov, R. A. Vicencio, and M. A. Gorlach, Nano Letters **25**, 4291 (2025).
[55] R. A. Vicencio, APL Photonics **10**, 071101 (2025).
[56] H.-R. Xia, Z. Wang, Y. Wang, Z. Gao, and M. Xiao, Phys. Rev. Lett. **135**, 176902 (2025), arXiv:2509.12843 [physics.optics].
[57] J. Yang, Y. Li, Y. Yang, X. Xie, Z. Zhang, J. Yuan, H. Cai, D.-W. Wang, and F. Gao, Nature Communications **15**, 1484 (2024).
[58] J. H. Kang, J. H. Han, and Y. Shin, New Journal of

Physics **22**, 013023 (2020).

[59] H. Li, Z. Dong, S. Longhi, Q. Liang, D. Xie, and B. Yan, Phys. Rev. Lett. **129**, 220403 (2022).

[60] M. M. Samak and O. R. Bilal, Phys. Rev. Lett. **133**, 266101 (2024).

[61] H. Wang, W. Zhang, H. Sun, and X. Zhang, Phys. Rev. B **106**, 104203 (2022).

[62] J. G. Martinez, C. S. Chiu, B. M. Smitham, and A. A. Houck, Science Advances **9**, eadj7195 (2023), arXiv:2303.02170 [quant-ph].

[63] T. Han, Z. Lu, Y. Yao, J. Yang, J. Seo, C. Yoon, K. Watanabe, T. Taniguchi, L. Fu, F. Zhang, and L. Ju, Science 10.1126/science.adk9749 (2024).

[64] Z. Lu, T. Han, Y. Yao, Z. Hadjri, J. Yang, J. Seo, L. Shi, S. Ye, K. Watanabe, T. Taniguchi, and L. Ju, Nature **637**, 1090 (2025).

[65] V. Brosco, L. Pilozzi, and C. Conti, Phys. Rev. B **104**, 024306 (2021).

[66] E. Wigner, *Group theory: and its application to the quantum mechanics of atomic spectra*, Vol. 5 (Elsevier, 1959).

[67] C. Córdova, P.-S. Hsin, N. Seiberg, and P.-S. Hsin, SciPost Physics **5**, 006 (2018).

[68] We denote the complex conjugate of a matrix $\boldsymbol{A}$ by $\boldsymbol{A}^*$.

[69] P. Heinzner, A. Huckleberry, and M. Zirnbauer, Commun. Math. Phys. **257**, 725 (2005).

[70] P. Sathe and R. Roy, Phys. Rev. B **111**, L041105 (2025), arXiv:2309.06487 [cond-mat.mes-hall].

[71] The choice of unit cell representation can be further fine-tuned in order to diagonalize H_0 in Eq. (1) while keeping $H_j^s = 0$. In this case, the ABF lattices are called Fully-Detangled.

[72] A triangular plaquette constitutes the minimal loop necessary to induce TRS breaking via magnetic field.

[73] R. Shankar, *Principles of Quantum Mechanics* (Springer US, 1994).

[74] D. Leykam, J. D. Bodyfelt, A. S. Desyatnikov, and S. Flach, Eur. Phys. J. B **90**, 1 (2017).

[75] J. Vidal, P. Butaud, B. Douçot, and R. Mosseri, Phys. Rev. B **64**, 155306 (2001).

[76] R. Khomeriki and S. Flach, Phys. Rev. Lett. **116**, 245301 (2016).

[77] A. Ramachandran, A. Andreanov, and S. Flach, Phys. Rev. B **96**, 161104(R) (2017).

[78] M. Gell-Mann, in *The Eightfold Way* (CRC Press, 2000).